

Article

Testing the Efficacy of Indirect Methods on Characterization of Sedimentary Basins by Correlation of Direct Data and Geophysical Techniques

Javier Rey ¹, Rosendo Mendoza ², M. Carmen Hidalgo ^{1,*} and Bruna Marinho ¹

¹ Department of Geology and CEACTEMA, Higher Polytechnic School of Linares, Technological Scientific Campus, University of Jaen, 23700 Linares, Spain; jrey@ujaen.es (J.R.); bmb00013@red.ujaen.es (B.M.)

² Department of Mechanical and Mining Engineering and CEACTEMA, Higher Polytechnic School of Linares, Technological Scientific Campus, University of Jaen, 23700 Linares, Spain; rmendoza@ujaen.es

* Correspondence: chidalgo@ujaen.es

Abstract: The information obtained from direct data (geological mapping and boreholes) and indirect techniques (reflection seismology, time-domain electromagnetics and magnetometry) is combined to analyse the northern limit of the Bailén basin (southeastern Spain). This Triassic–Neogene basin is confined by a graben-type structure, limited by two normal faults in the SW–NE direction (the Baños de la Encina-La Carolina fault and Guarromán fault). The movement of these faults was complex, with different pulses occurring over time. Therefore, the subsidence of the basin and the sedimentary filling of the graben were different, giving rise to lateral changes in the facies and thicknesses. This study focuses on the Baños de la Encina fault, chosen as the experimental site to analyse the effectiveness and accuracy of these geophysical techniques to reveal the basement structure and geometry. Seismic reflection allows to detect two faults that caused the subsidence of the eastern sector of the graben. The TDEM method made it possible to calculate the depth of the Palaeozoic basement, as well as reveal the presence of the two aforementioned faults. Magnetic total field data highlight variations in the basement depth that can be used to infer previously unknown fractures, in this case, in the NW–SE direction.

Keywords: fault detection; seismic reflection; time-domain electromagnetics; magnetometry; Spain



Citation: Rey, J.; Mendoza, R.; Hidalgo, M.C.; Marinho, B. Testing the Efficacy of Indirect Methods on Characterization of Sedimentary Basins by Correlation of Direct Data and Geophysical Techniques. *Appl. Sci.* **2024**, *14*, 7308. <https://doi.org/10.3390/app14167308>

Academic Editors: Paulo T. L. Menezes and Valeria Barbosa

Received: 18 July 2024

Revised: 14 August 2024

Accepted: 16 August 2024

Published: 19 August 2024



Copyright: © 2024 by the authors. Licensee MDPI, Basel, Switzerland. This article is an open access article distributed under the terms and conditions of the Creative Commons Attribution (CC BY) license (<https://creativecommons.org/licenses/by/4.0/>).

1. Introduction

There are many examples of the application of different geophysical techniques in geological-mining research. The most commonly used techniques include gravimetric, magnetic, electrical, electromagnetic and seismic methods. However, these indirect techniques include a data inversion process, which generates uncertainty in the interpretation of these data (inverse problem). The solution to the inverse problem is not unique, since the same set of field data supports a domain of valid mathematical solutions, and modifications can be made in the measured property (e.g., resistivity) and in the thicknesses of the geological unit with the same measurement results [1]. For this reason, it is advisable to combine indirect techniques that measure different properties and whose results have a good geological significance depending on the direct information available [2–5].

In this work, the capacities of different geophysical techniques to study geological structures are analysed. For this purpose, the northern boundary of the detrital aquifer of Bailén (southeastern Spain, Figure 1a), characterized by the presence of normal faults in a NE–SW direction with several hundred meters of vertical displacement, was selected as the experimental site. The following two geophysical techniques that measure different properties (elasticity and conductivity) and offer good resolution at several hundred metres depth are used together: seismic and electromagnetic techniques (time-domain electromagnetic (TDEM) method). As a complementary geophysical technique, the magnetic method was

chosen. Although its use in the study of fractures is not as frequent in the literature as the previous ones, it was expected that it will provide additional information, such as the strike of the fractures existing in the subsoil and covered by recent materials. In addition, direct field information and groundwater catchment data were available, providing verification and correlation tools for the indirect techniques used in this work.

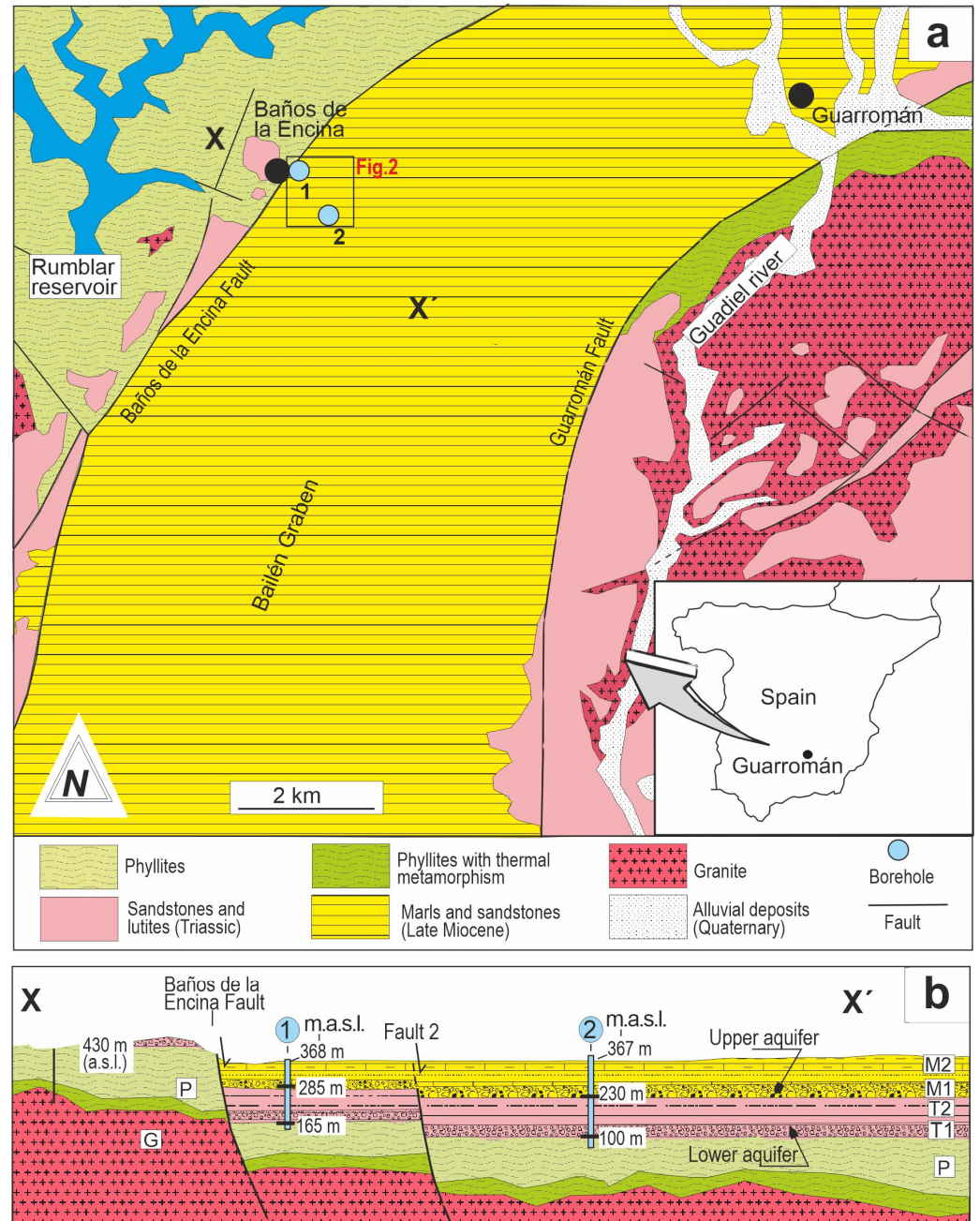


Figure 1. (a) Geographical location and geological map of the Bailén basin. The studied sector is indicated (black box, see Figure 2), as are the positions of two boreholes (1 and 2) and the location of the X–X' section. (b) X–X' geological section, which includes the positions of boreholes 1 and 2. G: granite, P: phyllites; T1: conglomerates and sandstones of the basal Triassic (lower aquifer); T2: lutites of the upper part of the Triassic; M1: rudites and calcarenites from the basal Miocene unit (upper aquifer); M2: marls from the upper part of the Miocene.

First of all, the information provided by seismic reflection is analysed and compared with stratigraphic data obtained in the field. Seismic methods are the most important

geophysical technique in terms of accuracy, resolution and penetration depth [1]. The main objective of seismic reflection is to provide information on the geological structures of the subsoil and to identify different boundaries through changes in the acoustic impedance of the materials passed through [6]. Reflection seismology is the most commonly used tool for establishing the fundamental structural and depositional framework, therefore it has been widely used in the analysis of sedimentary basins and in hydrocarbon exploration [7–10].

Second, the time-domain electromagnetic method (TDEM) is applied in this study. The TDEM operating principle consists of circulating an electric current through a transmitting coil for short periods of time. When the flow of current is abruptly interrupted, a variation in the primary magnetic field occurs, which induces a variable electric current. This, in turn, generates a transient secondary magnetic field. These currents flow in closed paths and migrate in depth, decreasing in intensity over time. Changes in the secondary magnetic field over time induce a transient voltage in the receiving coil. The decay of this voltage provides information on the distribution of the subsoil conductivity, which can be used for its characterization [11,12]. This geophysical prospecting technique is used for many tasks. Although this method was originally used in the prospecting of deep mineral deposits [12], its ability to detect changes in conductivity associated with variations in the salinity of aquifers was later confirmed. This led to its widespread use in the investigation of marine intrusions in coastal areas [13–16] or in the detection of pollution plumes in environmental studies [17]. It has also been used in the analysis of sedimentary basins, in particular, to detect the depth of the base under sedimentary coverings [3,4,18,19].

In addition, the information that magnetic techniques can provide in this geological context is analysed and compared with the above-mentioned methods. Magnetic prospecting is based on the detection of anomalies in the Earth's magnetic field. These anomalies are caused by materials that present high magnetic susceptibility; that is, they can be magnetically polarized in the presence of an inductive field [1]. Before these measurements can be interpreted, the influence of external fields (basically the diurnal variations in the magnetic field) must be considered. This methodology has been extensively described in the literature [1,6,20] and it is widely used in different fields of Earth science. In mining, this method has proven useful in prospecting for ferromagnetic materials [21–25] and in hydrocarbon prospecting, providing information on deep structures that can function as traps [26]. It has also been used as a complementary tool for geological mapping [27,28], locating faults in covered areas [29,30].

In this study, the information provided by the surface geological survey and the data from boreholes is compared with the results obtained through geophysical prospecting. This will allow, on the one hand, to complement the geological information of this sedimentary basin, as well as the characterization of the related aquifers. On the other hand, the comparison of the results obtained with the different indirect techniques used (seismic reflection, TDEM and magnetic) allow us to analyse the effectiveness of each of them in this geological context.

2. Geological Setting

2.1. Regional Geological Context

In the studied region, the following two geological units can be distinguished: the Palaeozoic basement and the sedimentary cover (Figure 1). The first unit is basically composed of intensely folded phyllites intruded by granite in the last stages of the Hercynian Orogeny [31,32]. Post-Hercynian sedimentary cover is deposited unconformably on this basement, arranged sub-horizontally. This cover is composed of Triassic, Miocene and Quaternary materials. The basal Triassic deposits are characterized by the presence of levels of fluvial conglomerates and sandstones that are wedged laterally, with abundant quartzite and sandstone clasts, that do not exceed 20 m in thickness (T1 in Figure 1b), according to the information obtained in the geological research carried out in the nearby outcrops, as well as the data provided in previous works [31]. Above these facies, there is a set of red lutites with some sandstone intercalations whose thickness ranges between

60 and 120 m, depending on the sector (T2 in Figure 1b) [31]. Above this set and separated by a stratigraphic discontinuity is the Late Miocene (Messinian) unit, with thicknesses of approximately 100–150 m in the sector but sometimes reaching 200–300 m towards the centre and south of the basin. At the base, calcarenitic breccias or polygenic conglomerates (M1 in Figure 1b) appear, which change laterally and vertically to marl and limestone marl with fine calcarenitic intercalations (M2 in Figure 1b) [31]. The Quaternary deposits are associated only with the filling of river channels and are characterized by the presence of silt, sand and gravel [31–33].

There are two subparallel normal faults (the Baños fault and Guarromán fault, Figure 1a), oriented NE–SW, that delimit a horst/graben structure. The differential erosion of these structures results in the sedimentary cover being conserved almost exclusively in the depressed sector (graben structure), which is known as the “Bailén Basin”.

The Bailén Basin is characterized by the presence of two superimposed aquifer units, which coincide with the basal Triassic materials (T1 in Figure 1b) and basal Late Miocene (M1 in Figure 1b). The lower aquifer offers low pumping flow rates (between 1–2 L/s), and the upper aquifer offers somewhat higher pumping rates (between 1 and 5 L/s). Laterally, these aquifers are limited by the two faults mentioned above. The movement of these faults was complex, with different pulses occurring over time [4]. Therefore, the subsidence and sedimentary filling of the basin were different, with lateral changes in facies and thicknesses, which in turn influenced both the hydrogeological characteristics of the units described and the discharge rates of the exploitation boreholes [33,34].

2.2. Local Geological Data

This study focused on the northern boundary of the Bailén Basin, which is in the vicinity of Baños de la Encina (Figures 1 and 2). At some points in this locality, the contact between the base of the Triassic and the Palaeozoic basement outcrops, in the horst block of the fault (Figures 1b and 2), at an elevation of 430 m (above sea level (asl)). In this area, geological information is provided by two groundwater exploitation boreholes. In addition to the information on the lithologies traversed, the thickness of the geological units and the heights of the lithological changes, they are used to calculate the velocities in the seismic profile analysed.

Towards the east, in the graben block and at an elevation of 368 m asl, a borehole was drilled (borehole 1 in Figures 1 and 2), in which the contact between the basal Miocene and the Triassic was reached at 83 m of drilling (285 m asl), and the base of the Triassic was reached at 203 m of drilling (165 m asl). From the difference in the elevation of the basal sedimentary cover on both sides of the Baños de la Encina fault in the vicinity of this locality, we estimate a throw of 265 m for this structure.

Approximately 700 m to the SE, another borehole was drilled for groundwater withdrawal (borehole 2 in Figures 1 and 2). In borehole 2, the contact between the sedimentary cover and the top of the Palaeozoic basement was reached at a depth of 267 m. Taking into account that the starting point was 367 m asl, the base of the Triassic unit was located at 100 m asl. By comparing the position of this level in the two soundings, the contact between the sedimentary cover and the Palaeozoic basement is deduced to be located 55 m below the previous one, which could be associated with a new fault (fault 2 in Figures 1b and 2) that would sink the SE sector.

The presence of these faults would be consistent with the aforementioned graben model and would justify the increase in thickness of the sedimentary cover towards the centre and south of the Bailén basin mentioned in some studies [32,33]. However, in the loamy facies (M2) that emerges on the surface, the presence of this structure has not been verified; therefore, this structure does not appear on geological maps.

In this work, different geophysical techniques (seismic reflection, time-domain electromagnetics and magnetometry) are used to corroborate the existence of this structure, as deduced from the direct data of the aforementioned surveys.

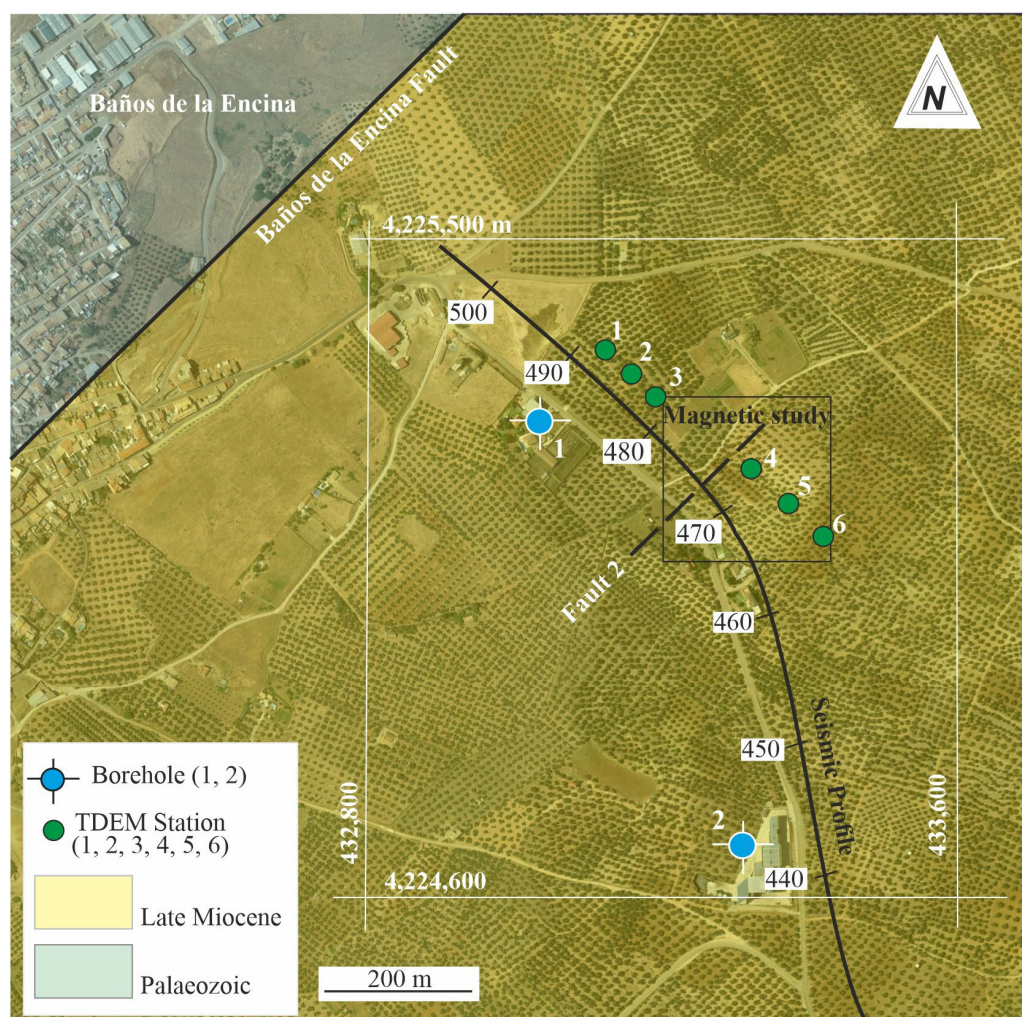


Figure 2. Details of the studied sector (black box in Figure 1a). The positions of fault 2, the boreholes (1 and 2), the different time-domain electromagnetic stations (1, 2, 3, 4, 5, 6) and the seismic profile with the positions of its traces are shown. Coordinates are in m.

3. Geophysical Survey

3.1. Seismic Reflection Transect

Seismic reflection profiles collected in the 1980s by the Geological and Mining Institute of Spain [35] were analysed. A Mini-Sosie vibrator was used as the seismic source, and model SM-7GR geophones with 30 Hz sensors were used to record the signals. An array of 18 geophones per trace was used, grouped in two lines parallel to the orientation of the profile, with 9 geophones each and with a separation between them of 1.85 m (the measurement was made by means of a double geophone in each position). The spacing between the traces was 15 m.

At each firing point, 2100 hits were generated. To fix the shooting distance, tests were carried out at 30, 45, 60 and 75 m. The best reflections were obtained at distances of 45 m.

The information was processed by the Compagnie Générale de Géophysique (CGG). The processing flow followed a standard sequence of processing, including collection of points in the “slalom line”, deconvolution prior to stacking, static corrections from ground level at the referred point to mean ground level (time origin), continuous velocity analysis, dynamic velocity correction, automatic adjustment of residual static corrections (SATAN), gains, bandpass filtering (3–100 Hz), coherence improvement, migration and analogical output of the information [35].

In this work, one of these seismic lines is used, namely, line 1 (see location in Figure 2). For the double-time/depth transformation, interval velocities of 1900 m/s were considered to the base of the Miocene unit, and an interval velocity of 2200 m/s were considered to the base of the Triassic unit. This velocity was determined in the processing of the line and was verified based on the known thicknesses of the different units according to mechanical probing performed in the area.

3.2. Time-Domain Electromagnetic (TDEM) Survey

The TDEM equipment used in this work was the AIE-2 model of the ELGEO Research & Production Company. This device has a maximum output power of 200 W and a current intensity of up to 10 A. The TDEM receiver is based on a 16-bit analogue–digital converter with a signal processor that provides an analogue–digital conversion immune to input voltage noise and real-time signal pre-processing [36].

In the field campaign, a total of six TDEM measurement stations were established in the NW–SE direction, coinciding with the seismic line analysed. The points located in Figure 2 indicate the centres of the reading stations for square loops of 100 and 200 m on each side. At each of these points, measurements were taken with central-loop and single-loop devices, and the measurement parameters (intensity, time and voltage) were varied, allowing the efficiency and stability of the different configurations to be compared. Thus, to reach research depths on the order of 200 m (at the first three stations), transmitter loops of 100×100 m were used. For the last three stations, which were designed to study the graben block of the fault, larger transmitter loops (200×200 m) were used since a greater Palaeozoic basement depth was expected. In all cases, a 6 mm² section cable was used, which reduces its resistance and, therefore, allows a higher effective current intensity to be achieved. At those stations in which a central loop device was used, the receiving coil had dimensions of 20×20 m and a loop of five turns. For the visualization and processing of the different curves, the software TEMBIN version 1.1 was used. The modelling and inversion process was carried out with the software ZondTEM1D version 1.1.

3.3. Magnetic Survey

In this study, field work was carried out with a GEM GSMP-35G v8.0 portable potassium magnetometer (GEM SYSTEMS, Markham, ON, Canada). This potassium magnetometer obtains high data quality due to its high sensitivity (0.0003 nT), minimum reading error, resolution (0.0001 nT) and high precision (± 0.05 nT). It has the capacity to take up to 20 readings per second, which provides a remarkable sampling density while walking [37]. Nineteen continuous profiles in the NW–SE direction were made in walking mode, with a length between 250–350 m and a separation between profiles of 10 m. Given the stability of the equipment used, measurements were taken every 50 ms. The georeferencing was carried out with a NovAtel GPS device mounted on the top of the mobile device.

To calculate the main magnetic field, the International Geomagnetic Reference Field (IGRF, 13th) calculator of the British Geological Survey (https://geomag.bgs.ac.uk/data_service/home.html, accessed on 24 March 2023) was used. Regarding the effect of external fields, diurnal correction was carried out. For this, data from the San Pablo Observatory of the National Geographic Institute (<https://www.ign.es/web/ign/portal/gmt-area-geomagnetismo>, accessed on 24 March 2023) were used.

To obtain the total field magnetic anomaly, the value of the main magnetic field (obtained with the IGRF model) was subtracted from the contributions of the external field (diurnal correction) and the values measured with the magnetometer at each point. Daytime correction and despiking were carried out using the software GEMLink version 5.4. The software Surfer was used for data interpolation and 2D representation. The data were analysed with different interpolation methods (kriging, cokriging, natural neighbour, nearest neighbour, etc.). Ultimately, kriging was selected as the interpolation method. The corresponding variogram showed the best fit with the maximum distance.

4. Results and Discussion

4.1. Seismic Reflection Survey

The trace of the seismic profile is perpendicular to the mapped Baños fault (Figures 1 and 2) that bound the Bailén Basin. Therefore, it is expected that it will allow the detection of other possible subparallel structures associated with the same fracturing system. In addition, the different mechanical behaviour of the lithologies studied should allow differentiating the described units, as well as deducing lateral thickness changes in the profile.

In the upper part of the seismic profile in Figure 3, materials attributable to the Miocene are represented in two shades of yellow (M1 + M2). At the base of this unit, there are levels that contain moderate-amplitude reflectors (M1), which are interpreted as sandstones and are related to the upper aquifer (Figure 3). The thicknesses obtained using an interval velocity of 1900 m/s [35] fit the depths to the base of the Miocene found in boreholes 1 and 2.

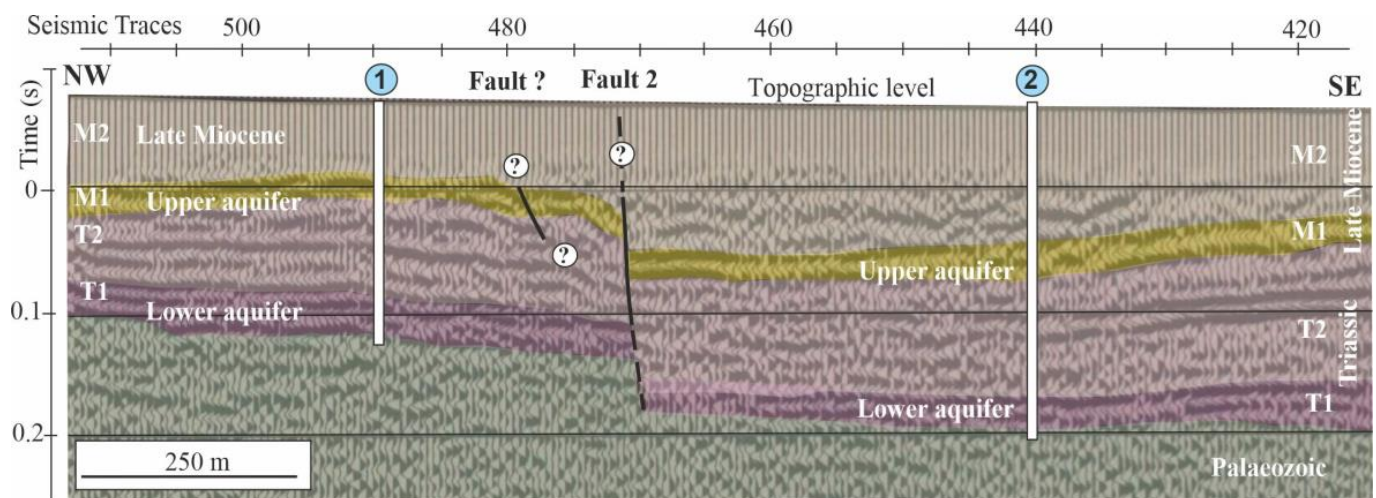


Figure 3. Seismic reflection profile and interpretation (see location in Figure 2). The positions of boreholes 1 and 2 are indicated. T1: conglomerate and sandstones of the lower Triassic (lower aquifer); T2: lutites of the upper Triassic; M1: rudites and calcarenites from the basal Miocene unit (upper aquifer); M2: marls from the upper Miocene.

Underlying the Miocene unit, the Triassic unit appears, represented in shades of pink in the seismic profile (Figure 3). One hundred seismic traces are represented, corresponding to 1500 m on the horizontal axis of the profile. This short distance is sufficient to detect changes in the thickness of the Triassic unit. At the NW end (trace 510), it covers a two-way time of 0.08 s, which corresponds to a thickness of 88 m (with an estimated interval velocity of 2200 m/s). In contrast, at the SE end (trace 420), the Triassic unit covers a greater two-way time, approximately 0.15 s, which is correlated with a thickness of 165 m. The estimated interval velocity to the base of the Triassic (2200 m/s) is verified in boreholes 1 and 2, where the thicknesses are 120 and 130 m, respectively.

Within the Triassic unit, maximum increase in wave amplitudes are also detected in the seismic trace, which are correlated with levels of sandstones and conglomerates. They are especially abundant at the base of the Triassic unit but also appear in the middle part (SE sector). The increase in wave amplitude associated to the Triassic base corresponds to the lower aquifer (T1 in Figure 3). Laterally, this base reflector may be lost due to changes in thickness or even due to the wedging of the basal conglomerates (between traces 460–470), as seen in outcrops in the northwestern sector of the Baños fault. In the lower part of the profile, the acoustic basement consists of the folded phyllites of the Palaeozoic basement, which are characterized by a discontinuous reflectivity, which generates chaotic features and disorganized seismic facies (Figure 3).

The seismic reflection profile in Figure 3 also shows a series of faults that affect the basement and the sedimentary cover. The most obvious difference is between seismic traces 470 and 475 (Fault 2 in Figure 3). The reflectors sink towards the SE by approximately 0.05 s, which corresponds to the 50 m throw detected in the two boreholes. This fracture affects the base and the sedimentary cover. Although the faults affect the Late Miocene and are, therefore, of a later age, the thickness changes in the Triassic suggest previous pulses that affected the subsidence and the sedimentation rate already in the Triassic. Furthermore, it should be noted that the lack of information in the first 0.06 s of the seismic profile makes it impossible to know if the highest part of the Miocene is also affected or, on the contrary, fossilizes the structure. This creates some uncertainty about the age of the last pulse of the fault.

In addition to this fault, the morphology of the reflectors suggests the presence of another fault with a smaller throw around seismic trace 490 (Figure 3). This structure affects the materials attributed to the upper part of the Triassic and to the base of the Miocene (M1), which sink slightly towards the SE. The lack of resolution in the upper part of the profile makes it difficult, also in this case, to establish whether the fracture affects the most recent materials and, therefore, whether it was before or after them. It is noteworthy that the materials of the lower part of the Triassic and the basement do not suffer vertical displacements associated with this fracture, which would not be coherent if it were a normal fault.

4.2. Time-Domain Electromagnetic (TDEM) Method

The TDEM campaign was designed after detecting fault 2 in the seismic profile and calculating the depths of the different units in both fault blocks. Three stations were positioned on each block of the fault (Figure 2). In the footwall block, loops of 100×100 m were used (stations 1, 2 and 3 in Figure 2); in the hanging wall block it was necessary to increase the size to 200×200 to be able to detect the Palaeozoic basement, since it is located at a greater depth (stations 4, 5 and 6 in Figure 2).

Figure 4 shows the curves generated at the six TDEM stations carried out in this study. The induced voltage curve measured in the field and that generated by the ZONDTEM1D version 1.1 software model are represented in blue. The red line represents the apparent resistivity curve obtained as a function of time and, likewise, that generated according to the software model. In addition, the resistivity model generated by the inversion software is represented by a thick red line. According to a comparison of the induced voltage curves at the different stations, a better fit is obtained for Stations 4, 5 and 6, where both curves coincide (the one generated with the field data and the one from the model proposed by the software). This is also the case for the apparent resistivity curves obtained with measured data and modelled data. The fit is worse for Stations 1, 2 and 3, where the two voltage curves coincide poorly, especially in the final part. This is reflected in the root-mean-square (RMS) error, with values of 0.5%, 0.7% and 0.3% for the measurements made at Stations 4, 5 and 6, respectively. In contrast, for Stations 1, 2 and 3, the RMS error values are high, on the order of 8%, 17% and 9%, respectively.

For Stations 1, 2 and 3, several sections are differentiated in the resistivity curves obtained after the inversion. These first measurements are associated with the M2 section, where the marly facies generate decreasing resistivity values. Occasionally, within this section, abrupt increases in resistivity are associated with calcarenitic intercalations in this unit. This is detected, for example, at Station 3 at a depth of about 50 m (Figure 4). The contact between the marly facies of M2 and calcarenites, breccias or polygenic conglomerates (M1) is very well evidenced in all curves by a sharp increase in resistivity at depths of 78 m, 79 m and 116 m at Stations 1, 2 and 3, respectively (Figure 4). The basal detrital section of the Miocene and the Triassic levels cannot be differentiated, so the set is represented as M1 + T in Figure 4. The last section of the curves corresponds to the Palaeozoic basement. In this case, the contact between the sedimentary cover and the basement is detected at all stations as a sudden increase in resistivity, at depths of 228 m, 232 m and 228 m at Stations 1, 2 and 3, respectively (Figure 4). If the elevation of the ground surface at each station and the depth measurements are taken into account, the elevations above sea level of this contact

are 145 m, 140 m and 141 m at Stations 1, 2 and 3, respectively (Figure 5). These results are very similar to the elevation of this same contact in borehole 1 (165 m asl). If these values are compared with the elevation of the Triassic base in the uplifted block (430 m asl), a vertical displacement of about 285 m is deduced for the Baños de la Encina fault. This value is similar to that calculated with the data from borehole 1 (265 m).

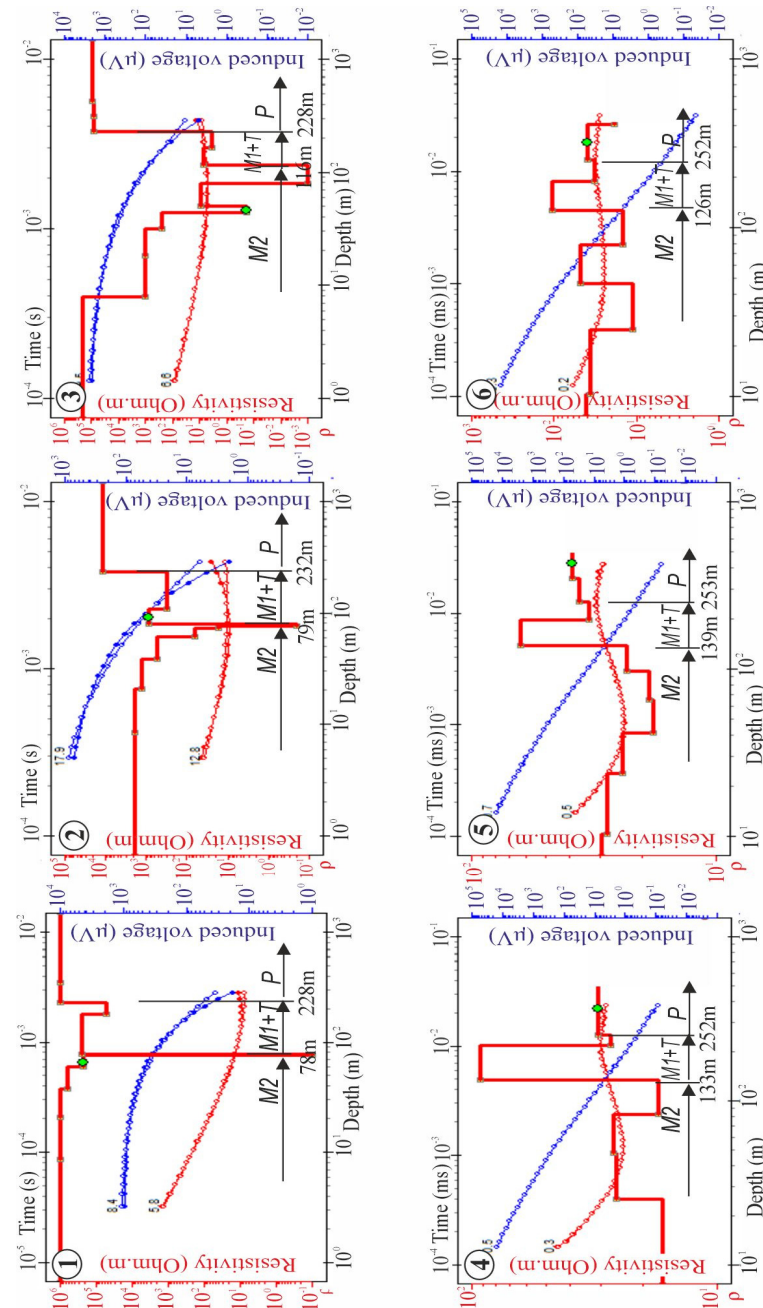


Figure 4. Induced voltage curves (blue lines) and apparent resistivity (red lines) as a function of time at the six TDEM stations (1, 2, 3, 4, 5 and 6). Two voltage lines are represented: one defined by circles filled in blue (field measured values) and the other by unfilled circles (model proposed by the software). In turn, two red lines are represented for apparent resistivity: one with circles filled (field measured values) and the other with unfilled circles (model proposed by the software). The interpretation after the inversion of the data is also included: the red straight lines represent the resistivity as a function of depth. P: Palaeozoic phyllites; T: Triassic; M1: rudites and calcarenites from the basal Miocene unit (upper aquifer); M2: marls from the upper Miocene unit.

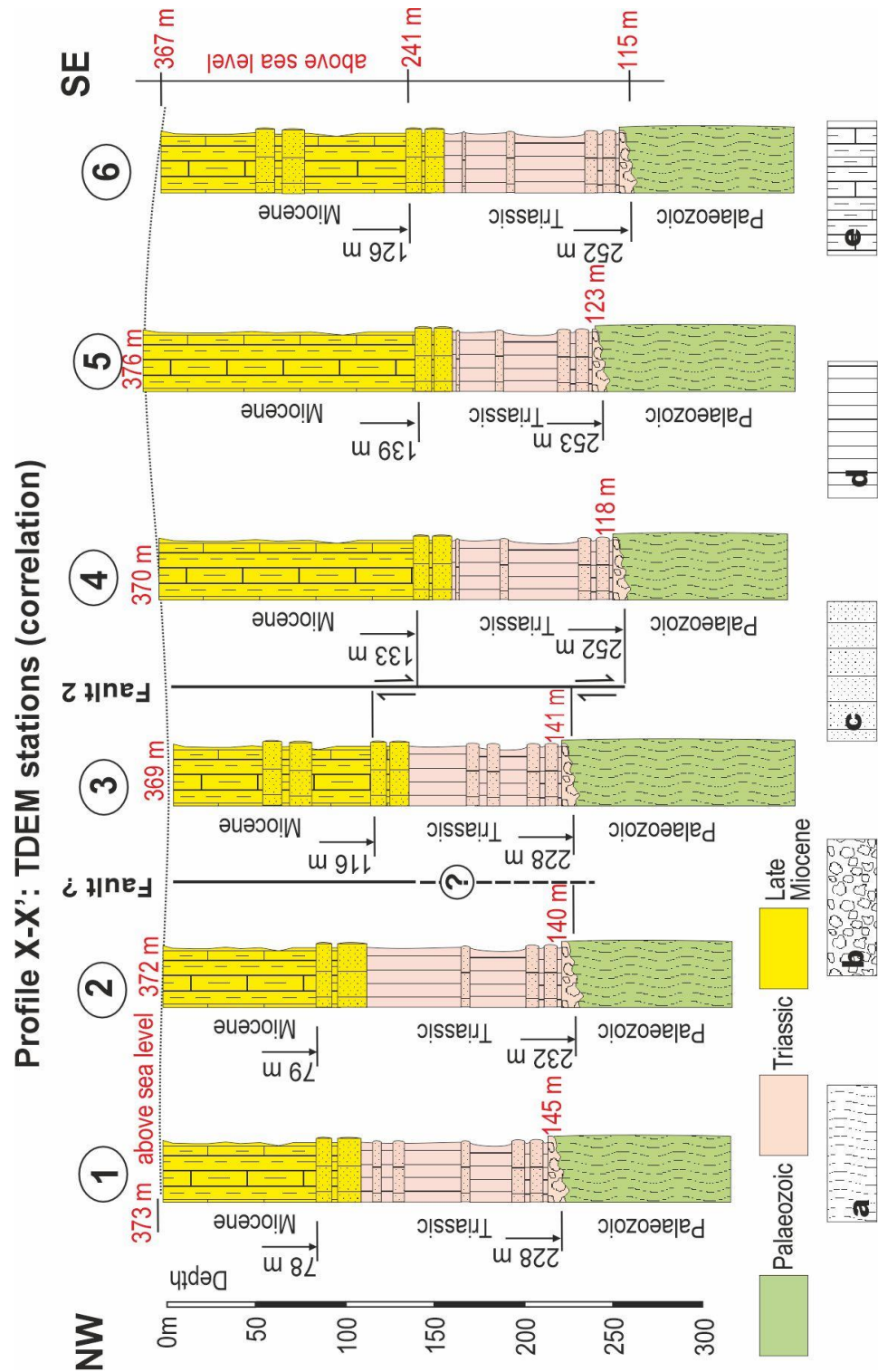


Figure 5. Stratigraphic columns deduced from the TDEM method information at each of the measurement stations (1, 2, 3, 4, 5 and 6). The numbering in black corresponds to the depths at which the reference levels were found (top of the basal Late Miocene calcarenite/conglomerate and base of the Triassic). The numbering in red corresponds to the elevation of the land surface at the point where the TDEM measurement was taken and to that of the two reference levels. a: folded phyllites; b: breccias or conglomerates; c: sandstones; d: lutites; e: marls and marly limestones.

At Stations 4, 5 and 6, the contact between assemblies M2 and M1 is characterized by a significant increase in resistivity associated with the top of the Miocene calcarenites, breccias or polygenic conglomerates. This contact was found at depths of 133 m, 139 m and 126 m at Stations 4, 5 and 6, respectively (Figure 4). If the values between Stations 1, 2 and 3 and Stations 4, 5 and 6 are compared, a vertical movement of approximately 50 m is obtained, which is consistent with the information provided by hydrogeological boreholes and the seismic profile. The contact of the sedimentary cover with the Palaeozoic basement is also associated, in this case, with a rise in resistivities at depths of 252 m, 253 m and 252 m (at the different stations shown in Figure 4). If the elevation of the terrain at each station and the depth measurements are considered, the elevations above sea level of this contact would be 118 m, 123 m and 115 m at Stations 4, 5 and 6, respectively (Figure 5). The elevation obtained for this contact using this geophysical technique is very similar to that derived from direct data in borehole 2 (100 m). Additionally, if the elevation data of the basement at the six stations are compared, the presence of fault 2 is also deduced by means of the TDEM method.

In Figure 5, the lithological columns deduced for each of these TDEM stations are correlated. They indicate the depth measurements up to the reference levels (in black), as well as the elevation of these surfaces above sea level (in red). If the TDEM X–X' profile (Figure 5) and the seismic profile of Figure 3 are compared, it can be noticed that fault 2 is detected by both techniques. Also, in both cases, another structure (Fault ? in Figures 3 and 5) is inferred, which is characterized by a deepening of the Miocene base (M1) that does not affect the height of the Palaeozoic basement.

4.3. Magnetic Prospecting

The magnetic profiles were made in the SE-NW direction, parallel to the seismic profile and perpendicular to the SW-NE faults, with the aim of detecting them (Figure 6). After the field campaign was performed and the diurnal correction of the data was applied, despiking was carried out to eliminate environmental noise in both sectors. To obtain the total field magnetic anomaly, the value of the main magnetic field (obtained through the IGRF model) was subtracted. The result is represented in Figure 6.

In the magnetic anomaly map of the total field, a magnetic anomaly direction of N30E is detected, on the order of 20 nT, which coincides with the trace of fault 2 deduced in the seismic profile. These are medium-wavelength magnetic anomalies (Figure 7). In other regions, equivalent anomalies have been associated to a mean-depth origin in the sedimentary basin [20]. Thus, as described in other studies [27–30], fractures affecting sedimentary basins bring in contact basement and sedimentary cover materials with different magnetic susceptibility values, which would justify these linear anomalies.

In addition to fault 2, another alignment (N60E) that corresponds to a minor order anomaly is detected (approximately 10 nT), which could coincide with the secondary fault detected in the seismic profile, as well as with the direction of the faults mapped in the Palaeozoic basement in sectors adjacent to that studied [31].

Furthermore, in the surface representation of Figure 6, isolated anomalies of small dimensions and short wavelengths can be seen, suggesting very shallow bodies [20]. They are especially abundant towards the NE of the sector studied, in the vicinity of the road (Figure 6). All these anomalies are associated with the existence on the surface of anthropic remains with ferromagnetic elements (observed in the outcrop during measurements) that generate these small magnetic dipoles.

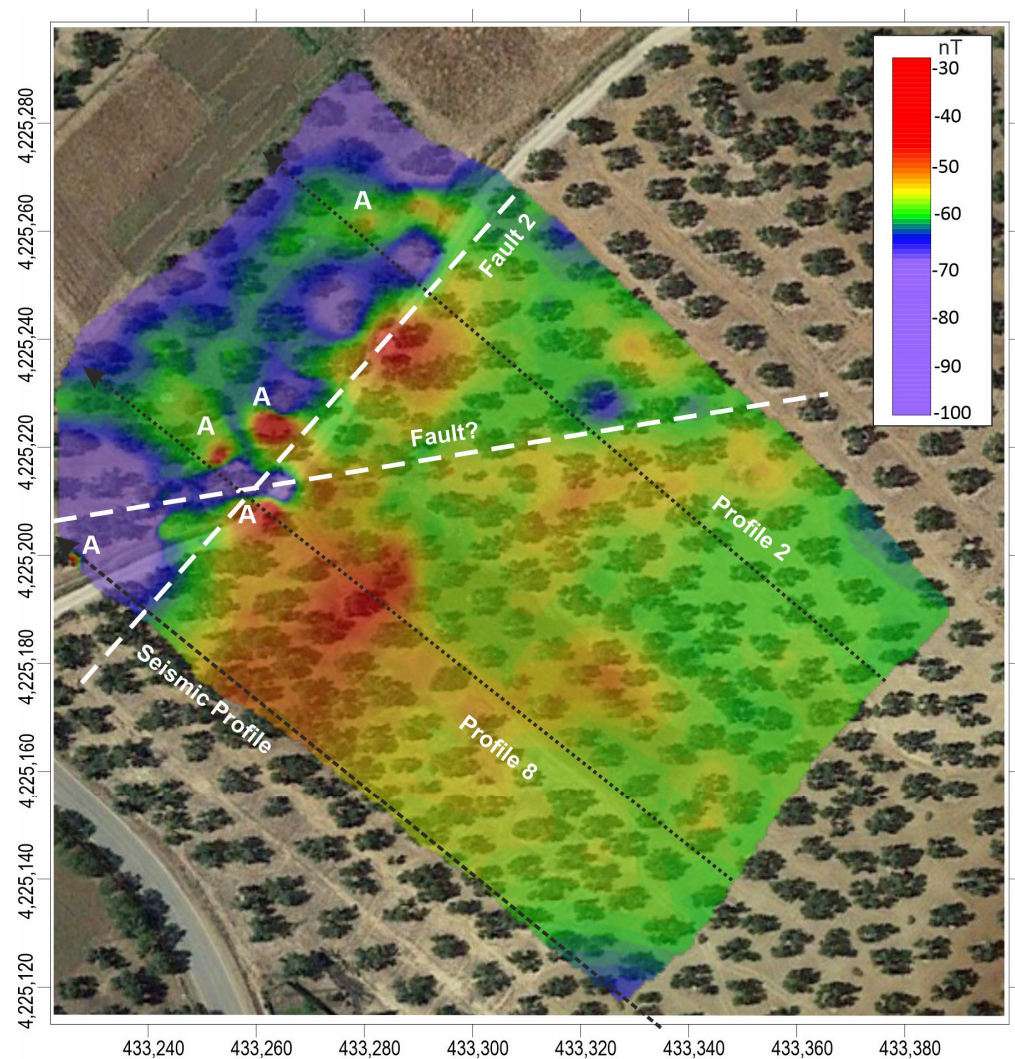


Figure 6. A map of the total field magnetic anomalies in the sector is shown in Figure 2. The positions of two of the magnetic profiles (2 and 8) are indicated, as well as the position of the seismic profile. A: small dipoles associated with ferromagnetic elements of an anthropic nature. Coordinates are in m.

Figure 7 shows two profiles of magnetic anomalies (Profile 2 and Profile 8), whose positions are indicated in Figure 6. In Profile 2, two anomalies associated with the two faults mentioned above are detected, where greater amplitudes are associated with fault 2. These two structures can be correlated with those indicated in the seismic profile of Figure 3. In Profile 8, as the two faults are very close, the magnetic anomalies appear to overlap. Anomalies of short wavelengths superimposed on the previous ones are also pointed out, suggesting very shallow bodies.

Like previous geophysical techniques, magnetic methods are capable of detecting faults that affect both the base and the sedimentary cover, even if they are not detectable in geological mapping. In addition, the orientation of the dipoles that form these magnetic anomalies allows us to find the strike of these structures, information that had not been obtained with seismic and TDEM techniques.

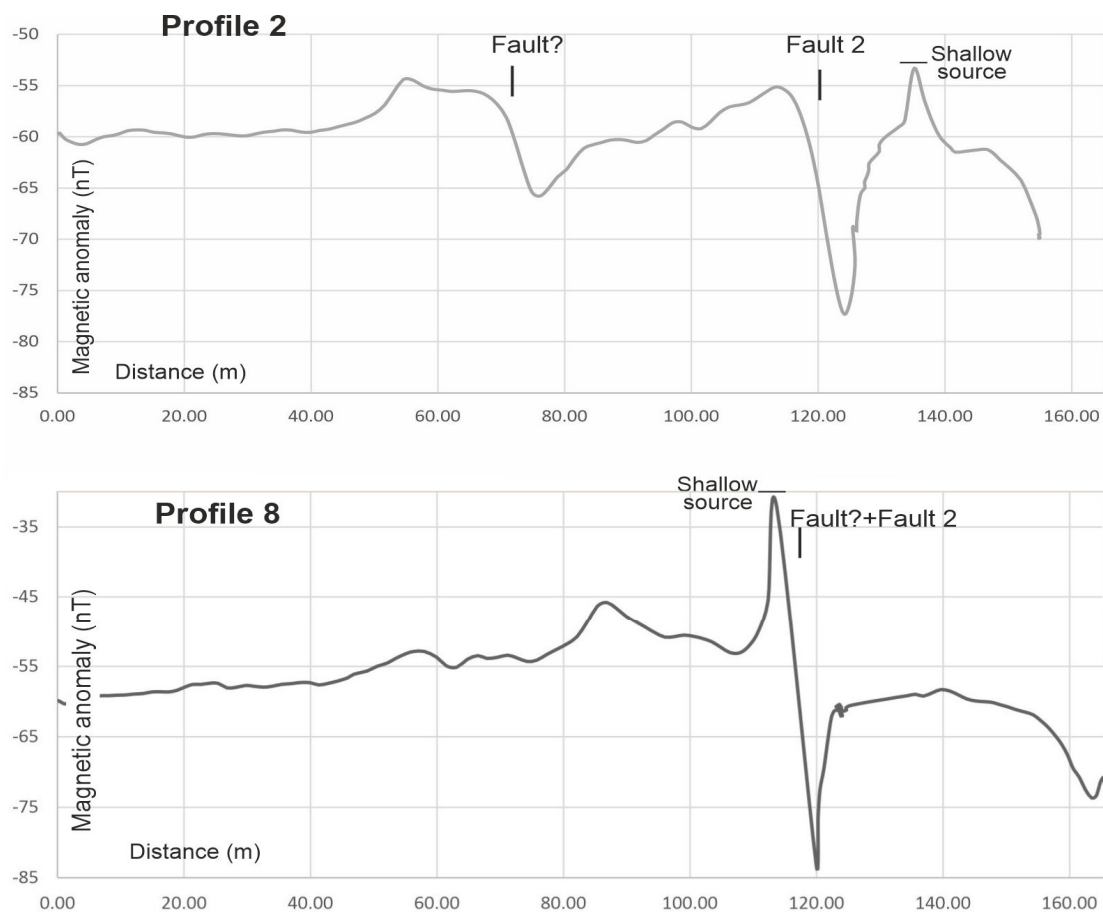


Figure 7. Total field magnetic anomaly profiles. Their positions are shown in Figure 6.

5. Conclusions

In this work, different direct and indirect methods were used in an integrated way to analyse the capacity of each method in the modelling of geological structures. For this purpose, the northern boundary of the Bailén basin in the vicinity of Baños de la Encina (southeast Spain) was chosen as study site. The following three different geophysical techniques were used: seismic reflection, time-domain electromagnetic (TDEM) and magnetic methods. These geophysical techniques were calibrated with available direct information, both from outcrop data and from boreholes.

The effectiveness of seismic reflection in characterizing sedimentary basins lies in its ability to provide high-resolution images of geological structures. In the seismic reflection profiles, abrupt changes are observed in the amplitude of the wave associated with the different lithologies of the sedimentary cover, as well as the acoustic basement associated with the Palaeozoic basement. By means of this method, two faults are detected that caused the subsidence of the eastern sector of the basin (the Bailén graben).

The TDEM technique is very versatile and can be used with different configurations and ranges of amplitude, voltage, time or device and loop size, depending on the depths at which the investigation is focused. Although its spatial resolution is lower compared to seismic reflection, it is a method that is easier to implement than the previous one. However, the interpretation of TDEM data requires complex mathematical models that do not provide a unique solution, so it requires the integration of the results obtained with other geophysical methods or direct geological data. In the case of TDEM, the best solution would be, a priori, the one that presents a better fit between measured and calculated data, characterized by low residual error values. The validation by means of direct geological data, from boreholes, and indirect data, obtained from the reflection

seismic profile, confirms the adequacy of the geoelectric model obtained. In this study, a good fit between the seismic and electromagnetic data was generally found. This method made it possible to locate the position of the upper aquifer, associated with calcarenites, breccias or polygenic conglomerates: the top of this unit is characterized by a sudden increase in resistivity values associated with these lithologies in comparison to the upper marls. However, the characterization of the lower aquifer under the Triassic clays was not so evident.

The TDEM method also made it possible to detect the depth of the Palaeozoic basement under the sedimentary cover, as well as the presence of the two aforementioned faults. The effectiveness of the TDEM analysis in calculating this depth is attributed to the notable resistivity contrast between the infilling materials and the underlying phyllitic basement rocks. This contrast in resistivity serves as a key parameter, enabling the differentiation and characterization of distinct geological layers also identified in the seismic reflection profile, thereby facilitating accurate depth assessments.

The magnetic method was chosen because of its efficacy to discern among rock bodies with different magnetic susceptibilities, and that provides a way of delineating subsurface geologic features as faults over broad areas. Magnetic prospecting revealed two alignments of anomalies in the geological map, which are associated with two fault phases (N30° E and N60° E). Both fault directions have been mapped in the boundaries of the Bailén basin when they affect the Palaeozoic basement, but they are not mappable in the Tertiary marly facies. These new data provide information on the orientation of linear structural features and allow to infer previously unknown faults.

Overall, a strong relationship is evident among the fractures inferred from seismic, electromagnetic and magnetic methods, indicating a robust fit between the different data sets. Therefore, the combined study of seismic, electromagnetic and magnetic techniques is of great interest in fracture analysis. The map of the magnetic anomalies and associated geophysical profiles across the study area show changes in bedrock depth and allow to infer concealed faults that are not observed at the surface.

Furthermore, this study allows us to better understand the complex fracturing phase of the northern boundary of the detrital aquifer associated with the Bailén basin. The obtained profiles of the basin show lateral and vertical variations in the bedrock topography, affecting both the hydrogeological behaviour of the units described and the discharge obtained by groundwater withdrawal. This is also important for other types of studies, e.g., for hydrogeological and geotechnical approaches.

Author Contributions: Conceptualization, J.R.; investigation, J.R., R.M., M.C.H. and B.M.; software, R.M. and J.R.; formal analysis, J.R., R.M. and M.C.H.; writing—original draft preparation, J.R.; writing—review and editing, M.C.H. All authors have read and agreed to the published version of the manuscript.

Funding: Grant PID2021-123506OB-I00 was funded by the MICIU/AEI/10.13039/501100011033 and ERDF/EU. This study was partly funded by the University of Jaen.

Institutional Review Board Statement: Not applicable.

Informed Consent Statement: Not applicable.

Data Availability Statement: The data that support the findings of this study are available upon request from the corresponding author.

Conflicts of Interest: The authors declare no conflicts of interest.

References

1. Telford, W.M.; Geldart, L.P.; Sheriff, R.E. *Applied Geophysics*; Cambridge University Press: Cambridge, UK, 1990; p. 770.
2. Martínez-Moreno, F.J.; Galindo-Zaldívar, J.; Pedrera, A.; Teixido, T.; Ruano, P.; Peña, J.A.; González-Castillo, L.; Ruiz-Constán, A.; López-Chicano, M.; Martín-Rosales, W. Integrated geophysical methods for studying the karst system of Gruta de las Maravillas (Aracena, Southwest Spain). *J. Appl. Geophys.* **2014**, *107*, 149–162. [[CrossRef](#)]

3. Rey, J.; Martínez, J.; Mendoza, R.; Sandoval, S.; Tarasov, V.; Kaminsky, K.; Hidalgo, M.C.; Morales, K. Geophysical characterization of aquifers in southeast Spain using ERT, TDEM, and vertical seismic reflection. *Appl. Sci.* **2020**, *10*, 7365. [CrossRef]
4. Mendoza, M.; Rey, J.; Martínez, J.; Hidalgo, M.C.; Sandoval, S. Geophysical characterisation of geologic features with mining implications from ERT, TDEM and seismic reflection (Mining District of Linares-La Carolina, Spain). *Ore Geol. Rev.* **2021**, *139*, 104581. [CrossRef]
5. Carrasco, J.; Carrasco, P.; Porras, D.; Martín, I. Drone Magnetic and Time Domain Electromagnetic Exploration in Metamorphic Formations: Tool for the Identification of Strategic Sites for Aquifer Exploitation. *Appl. Sci.* **2023**, *13*, 10949. [CrossRef]
6. Reynolds, J.M. *An Introduction to Applied and Environmental Geophysics*; John Wiley and Sons Ltd.: London, UK, 2011; p. 796.
7. Radwan, A.A.; Nabawy, B.S.; Shihata, M.; Leila, M. Seismic interpretation, reservoir characterization, gas origin and entrapment of the Miocene-Pliocene Mangaa C sandstone, Karewa Gas Field, North Taranaki Basin New Zealand. *Mar. Pet. Geol.* **2021**, *135*, 105420. [CrossRef]
8. Olutoki, J.O.; Siddiqui, N.A.; Haque, A.-E.; Akinyemi, O.D.; Mohammed, H.S.; Bashir, Y.; El-Ghali, M.A.K. Integrated analysis of wireline logs analysis, seismic interpretation, and machine learning for reservoir characterisation: Insights from the late Eocene McKee Formation, onshore Taranaki Basin, New Zealand. *J. King Saud Univ. -Sci.* **2024**, *36*, 103221. [CrossRef]
9. Hu, Y.; Liu, W.; Wang, J.; Zhang, G.; Zhou, Z.; Han, R. Basin-scale structure control of Carlin-style gold deposits in central Southwestern Guizhou, China: Insights from seismic reflection profiles and gravity data. *Ore Geol. Rev.* **2017**, *91*, 444–462. [CrossRef]
10. Jenkins, A.P.; Torvela, T. Basin analysis using seismic interpretation as a tool to examine the extent of a basin ore ‘play’. *Ore Geol. Rev.* **2020**, *125*, 103698. [CrossRef]
11. Nabighian, N.M. *Electromagnetic Method in Applied Geophysics*; Society of Exploration Geophysics: Tulsa, OK, USA, 1988; p. 971.
12. McNeill, J.D. *Principles and Application of Time Domain Electromagnetic Techniques for Resistivity Sounding*; Technical Note TN-27; Geonics Ltd.: Toronto, ON, Canada, 1994. Available online: <http://www.geonics.com/pdfs/technicalnotes/tn27.pdf> (accessed on 10 April 2023).
13. Danielsen, J.E.; Auken, E.; Jorgensen, F.; Sondergaard, V.; Sorensen, K. The application of the transient electromagnetic method in hydrogeophysical survey. *J. Appl. Geophys.* **2003**, *53*, 181–198. [CrossRef]
14. Kafri, U.; Goldman, M. Are the lower subaquifers of the Mediterranean coastal aquifer of Israel blocked to seawater intrusion? Results of a TDEM (time domain electromagnetic) study. *Isr. J. Earth Sci.* **2006**, *55*, 55–68. [CrossRef]
15. Farag, K.S.I.; Howari, F.M.; Abdelmalik, K.W. Imaging of Hydrothermal Altered Zones in Wadi Al-Bana, in Southern Yemen, Using Very Low Frequency–Electromagnetic and Remote Sensing Data. *Arab. J. Geosci.* **2019**, *12*, 554. [CrossRef]
16. Zhu, Z.; Shan, Z.; Pang, Y.; Wang, W.; Chen, M.; Li, G.; Sun, H.; Revil, A. The transient electromagnetic (TEM) method reveals the role of tectonic faults in seawater intrusion at Zhoushan islands (Hangzhou Bay, China). *Eng. Geol.* **2024**, *330*, 107425. [CrossRef]
17. Hallbauer-Zadorozhnaya, V.Y.; Stettler, E. Time Domain Electromagnetic Sounding to delineate hydrocarbon Contamination of Ground Water. In *Symposium on the Application of Geophysics to Engineering and Environmental Problems*; Environmental & Engineering Geophysical Society: Denver, TX, USA, 2009; pp. 241–251.
18. Sridhar, M.; Markandeyulu, A.; Chaturvedi, A.K. Mapping subtrappean sediments and delineating structure with the aid of heliborne time domain electromagnetics: Case study from Kaladgi Basin, Karnataka. *J. Appl. Geophys.* **2017**, *136*, 9–18. [CrossRef]
19. Bense, V.F.; Person, M.A. Faults as conduit-barrier systems to fluid flow in siliciclastic sedimentary aquifers. *Water Resour. Res.* **2006**, *42*, 1–18. [CrossRef]
20. Blakely, R. *Potential Theory in Gravity and Magnetic Applications*; Cambridge University Press: Cambridge, UK, 1995; p. 441.
21. Abdelazeem, M.; Gobashy, M.M. A solution to unexploded ordnance detection problem from its magnetic anomaly using Kaczmarz regularization. *Interpretation* **2016**, *4*, 61–69. [CrossRef]
22. Abedi, M.; Fournier, D.; Devriese, S.; Oldenburg, D.W. Integrated inversion of airborne geophysics over a structural geological unit: A case study for delineation of a porphyry copper zone in Iran. *J. Appl. Geophys.* **2018**, *152*, 188–202. [CrossRef]
23. Benítez, M.E.; Prezzi, C.; Benallivián Justiniano, C.A.; Verdecchia, S.O.; De Martino, F.J.; Carlini, M.; Lanfranchini, M.E. Ground magnetic survey and 3D geophysical model of ultrabasic rocks from the Martín García Complex (Buenos Aires, Argentina). *J. S. Am. Earth Sci.* **2023**, *121*, 104117. [CrossRef]
24. EldougDoug, A.; Abdelazeem, M.; Gobashy, M.; Abdelwahed, M.; Abd El-Rahman, Y.; Abdelhalim, A.; Said, S. Exploring gold mineralization in altered ultramafic rocks in south Abu Marawat, Eastern Desert, Egypt. *Abstr. Sci. Rep.* **2023**, *13*, 7293. [CrossRef]
25. Aminu, M.B.; Adiat, K.A.N.; Akinlalu, A.A.; Olomo, K.O.; Owolabi, T.O.; Aliyu, E.O. A review on the applications of airborne geophysical and remote sensing datasets in epithermal gold mineralisation mapping. *Geosyst. Geoenviron.* **2024**, *3*, 100284. [CrossRef]
26. Okiwelu, A.A.; Obianwu, V.I.; Eze Ohara, E.; Ude, I.A. Magnetic anomaly patterns, fault-block tectonism and hydrocarbon related structural features in the Niger Delta basin. *IOSR J. Appl. Geol. Geophys. (IOSR-JAGG)* **2014**, *2*, 31–46.
27. Nabighian, M.N.; Grauch, V.J.S.; Hansen, R.O.; LaFehr, T.R.; Li, Y.; Peirce, J.W.; Phillips, J.D.; Ruder, M.E. The historical development of the magnetic method in exploration. *Geophysics* **2005**, *70*, 33ND–61ND. [CrossRef]
28. Alva-Valdivia, L.M.; Guerrero-Díaz, P.; Urrutia-Fucugauchia, J.; Agarwal, A.; Caballero-Miranda, C.I. Rock-magnetism and magnetic anomaly modelling of Las Truchas, case study. *J. S. Am. Earth Sci.* **2020**, *97*, 102409. [CrossRef]
29. Akinlalu, A.A.; Adelusi, A.O.; Olayanju, G.M.; Adaiat, K.N.; Omosuyi, G.O. Aeromagnetic mapping of basement structures and mineralization characterization of Ilesa Schist Belt, Southwestern Nigeria. *J. Afr. Earth Sci.* **2018**, *138*, 383–391. [CrossRef]

30. Bouzekraoui, M.; Es-Sabbar, B.; Karaoui, B.; Essalhi, M.; Saadi, M. Structural analysis, tectonic fracturing modeling, and kinematic evolution along the South Atlas Fault at the northern border of the Tinghir-Errachidia-Boudenib basin (Pre-African Trough, Morocco). *J. Afr. Earth Sci.* **2024**, *212*, 105193. [[CrossRef](#)]
31. Castelló, R.; Orviz, F. *Mapa Geológico de España 1:50.000, Hoja nº 884 (La Carolina)*; Instituto Geológico y Minero de España: Madrid, Spain, 1976.
32. Larrea, F.J.; Carracedo, M.; Ortega Cuesta, L.; Gil Ibarguchi, J.I. El Plutón de Linares (Jaén): Cartografía, petrología y geoquímica. *Cuad. Lab. Xeológico Laxe Coruña* **1994**, *19*, 335–346.
33. Martín Parra, L.; Matas, J.; Roldán, F.J.; Martín-Serrano, A. *Mapa Geológico y Memoria Explicativa de la hoja 70 (Linares), Escala 1:200.000*; Instituto Geológico y Minero de España: Madrid, Spain, 2015.
34. I.T.G.E. *Atlas Hidrogeológico de la Provincial de Jaén*; Diputación Provincial de Jaén: Jaén, Spain, 1997; p. 260.
35. I.G.M.E. *Exploración Geológico-Minera de la Fosa Tectónica de Bailén (Jaén)*; Sísmica de reflexión; Ministerio de Industria y Energía: Madrid, Spain, 1983; p. 64.
36. AIE-2 Instruments. Available online: <http://zond-geo.com/english/services/equipment/aie-2-instruments/> (accessed on 1 August 2024).
37. GEM Systems. Available online: <https://www.gemsys.ca/ultra-high-sensitivity-potassium/> (accessed on 1 August 2024).

Disclaimer/Publisher’s Note: The statements, opinions and data contained in all publications are solely those of the individual author(s) and contributor(s) and not of MDPI and/or the editor(s). MDPI and/or the editor(s) disclaim responsibility for any injury to people or property resulting from any ideas, methods, instructions or products referred to in the content.